Liquid-vapor Growth of Atomically Thin Metal Tellurides with Controllable Polymorphism

Lin Zhou (linzhou@mit.edu)
Massachusetts Institute of Technology
Xingxing Zhang
Shanghai Jiao Tong University
Xu Zhang
Carnegie Mellon University
Yimo Han
Cornell University
Pin-Chun Shen
Massachusetts Institute of Technology
Yuxuan Lin
UC Berkeley https://orcid.org/0000-0003-0638-2620
Qingqing Ji
Massachusetts Institute of Technology
Ya-Qing Bie
Sun Yat-sen University
Jiaojian Shi
Massachusetts Institute of Technology https://orcid.org/0000-0002-1703-6363
Ahmad Zubair
Massachusetts Institute of Technology https://orcid.org/0000-0001-9827-3557
Xiaochuan Dai
Massachusetts Institute of Technology
Nan Yao
Princeton University https://orcid.org/0000-0002-4081-1495
Tomás Palacios
Massachusetts Institute of Technology
Jing Kong
Massachusetts Institute of Technology

Physical Sciences - Article

Keywords: thin transition metal dichalcogenides (TMDs), polymorphism

Posted Date: February 16th, 2021

DOI: https://doi.org/10.21203/rs.3.rs-225513/v1

Abstract

Atomically thin transition metal dichalcogenides (TMDs), together with their polymorphism, provide promising alternatives for next generation electronic devices and a platform to explore exotic quantum phenomena. However, a large-scale synthesis method that can reliably produce high-quality two-dimensional (2D) TMDs with controlled phase is still lacking. Instead, TMDs with high concentration of defects and defect-stabilized metastable crystalline phases are often obtained via conventional chemical vapor deposition. Here we developed a liquid-vapor (LV) technique to exploit liquid precursors to significantly suppress the equilibrium shift to the decomposition direction and successfully synthesized high-quality TMDs. We highlight the importance of exploiting the synergism of equilibrium and kinetics to facilitate the synthesis reaction (forward) and to impede decomposition (reverse). A high concentration of reactants in the liquid phase also maximizes the kinetic rate of defect repairing. We demonstrated the advantages of LV method by synthesizing diverse high-quality 2D metal tellurides with controllable polymorphs, which would be challenging, if not impossible, to realize by using conventional methods due to weak metal-tellurium bonds, thermal instability and the co-existence of mixed crystalline phases. In particular, we successfully synthesized high-quality monolayer 2H $MoTe_2$, which is only possible when Te defect level is substantially suppressed. Our approach provides a new paradigm in high-quality and large-scale materials synthesis and can be readily extended to a variety of quantum materials, potentially accelerating both research and industrial initiatives.

Main Text

As the silicon complementary metal–oxide–semiconductor (CMOS) technology scaling, driven by the Moore's Law, is running out of steam, atomically thin semiconducting TMDs, together with their polymorphism, provide promising alternatives for next-generation electronic devices [1-4]. Despite their huge potential and a decade of development, 2D TMD materials still remain an early-stage technology [4]. One important reason is the lack of a large-scale synthesis method that can reliably produce high-quality 2D TMDs with controlled phase and layer number [5]. At present, layered TMDs are typically synthesized by chemical vapor deposition (CVD) methods with a vapor-solid-solid (VSS) mode, in which solid precursors become vaporized, transported by gas flow, attach onto the solid substrates, then diffuse to bond with solid products [6,7]. However, such a VSS mode can only supply a limited amount of vapor precursor species nonuniformly because of a significant vapor concentration drop along the direction of gas flow [8]. This thermodynamically favors decomposition of the as-synthesized TMD compounds, and therefore drives defect creation during the CVD synthesis. As a result, high concentration of defects, and defect-stabilized metastable crystalline phases instead of pure defect-free phase are often obtained *via* VSS growth (Fig. 1a, right). This makes the phase control of monolayer even more challenging. Even worse, certain members of TMDs, especially for those with natural thermal instability, simply cannot be synthesized by the existing CVD methods. For instance, the CVD synthesis of monolayer 2H $MoTe_2$ is still missing owing to the defect-triggered phase transition from 2H to 1T' [2].

In order to address these challenges, here we present a new liquid-vapor (LV) synthesis mechanism and take full advantage of liquid phase of precursors to synthesize TMDs. Unlike the conventional VSS or other solid precursor-based CVD methods, liquid precursors are introduced as a reservoir, providing sufficient amounts of active species that significantly facilitate the synthesis reaction of TMDs and suppress the decomposition of the target TMD compounds. Even for TMDs with as-formed defects, the sufficient reactants provided in such a LV mode maximize the chance of defects repairing at high temperature. Therefore, the LV method is expected to produce high-quality 2D TMDs, and enable synthesis of TMDs with controlled phases that are unattainable via conventional VSS method.

We experimentally tested this LV method by using metal tellurides as a case study. 2D metal tellurides are highly attractive for topological physics and phase engineering due to their strong spin-orbit coupling and polymorphism [9-12]. The phase versatility of metal tellurides can greatly facilitate phase engineering such as phase heterostructure [2,13] and phase transition [12], which are promising for device applications, including high-performance 2D transistors with ohmic contact, topological transistors, reconfigurable circuits and memory devices, etc. Despite their great potential, the low electronegativity of tellurium and the weak metal-telluride bonds make this family of 2D TMDs particularly vulnerable to the undesirable chemistry in the VSS mode of CVD processes. Moreover, the tendency of decomposition and oxidation often leads to very defective synthesis, and for many cases, even a complete failure. In addition, 2D metal tellurides exhibit diverse polymorphs with similar formation energies, which makes the precise phase control even more challenging. To our knowledge, CVD grown monolayer 2H $MoTe_2$ (with phase control) has not been reported before.

In this work, we experimentally demonstrated that the proposed LV method was successful in synthesizing diverse high-quality metal telluride, particularly $MoTe_2$, with precise phase and layer-number control. Furthermore, main element tellurides flakes (SnTe and GaTe) were also synthesized through the LV approach. Our experimental findings have unveiled a new LV-facilitated process with on-site nucleation and on-demand reactant supply in the liquid phase, which is fundamentally distinctive from the conventional VSS process. As a general phase-guided method, this LV method can be applied to a wide range of precursors and material systems.

The merits of LV method can be understood from both kinetic and thermodynamic perspectives. The CVD synthesis involves two reaction processes: (1) formation: M (g) +xTe (l) MTe_x (s); and (2) decomposition: MTe_x (s) $MTe_{(x-y)}$ (s) + yTe (g) (M is metal), as shown in Fig. 1a. We highlight the vital role of decomposition as it is inevitable in conventional CVD growth, and is evidenced by defects and lattice disturbance in CVD-grown 2D metal tellurides (Supplementary Fig. 1). In order to synthesize high-quality materials, it is crucial to promote the formation process and impede the decomposition process. We use the LV strategy to exploit the synergism of equilibrium and kinetics to achieve this goal. From the kinetics point of view, the reaction rate of formation process sensitively depends on the precursors' concentration. It can be expressed as , where is the rate constant, c(M) and c(Te) denote the concentration of metal-based and tellurium precursors, respectively. Thus, a higher concentration of Te

will boost the kinetic growth rate ( ) of 2D metal tellurides. From a thermodynamics point of view, high concentration of Te will impede the decomposition of as-grown tellurides, thus minimize the probabilities of defect creation, and shift the equilibrium to the side of repairing defects according to the Le Châtelier's principle. For the LV growth, liquid reservoirs of Te supply a significantly higher concentration of on-site Te precursors than Te vapor in the conventional VSS method, since the Te concentration severely drops along the direction of the gas flow. Since the rate of defects repairing follows a power law against the concentration of Te, high concentration for liquid Te ensures fast repairing rate, which forms stoichiometric 2D tellurides without vacancies. In contrast, for the VSS mode, because of insufficient supply of Te, the growth rate of MTe_x should be much slower, and the as-grown MTe_x is prone to decompose, thus generating defects (Fig. 1a, right). In short, owing to sufficient reactants in liquid, the LV strategy can greatly facilitate growth, and minimize defects through the kinetic and thermodynamic control.

The process of LV growth is illustrated in Fig. 1b. Pre-deposited Te precursor begins to melt and forms liquid droplets when the furnace temperature is ramped up above the Te melting temperature (~450 ℃) (Fig. 1b, ii). Subsequently, as the metal precursor species vaporize, the Te liquid reservoir continuously collects surrounding gaseous precursor species (Fig. 1b, iii). The liquid-vapor-solid triple junction (solid is the substrate) is the major growth front. MTe_x continuously precipitates out at the liquid-solid interface (Fig. 1b, iv and Fig. 1c). As the growth proceeds, droplet vaporizes and the triple phase line moves inward (Fig. 1b, v and Fig. 1d). Consequently, the MTe_x flake has inward growth at the triple phase junction, and the growth terminates when the droplet is all consumed (Fig. 1b, vi and Fig. 1e). Simultaneously, the flake grows outward and increase lateral size through attachment of Te atoms from the in-situ saturated Te vapor and metal precursor atoms at the growing edge. Liquid precursor provides nucleation site and boosts growth. Moreover, liquid reservoir prevents defects generation and decomposition by continuously providing sufficient Te precursor in-situ during the growth.

Several experimental phenomena in the synthesis of metal tellurides are in good agreement with the proposed LV mechanism. Optical Microscope (OM) images illustrate several key stages during the LV growth of $MoTe_2$ (Fig. 1, c to e). The droplet-shaped particles were found on $MoTe_2$ flakes when the growth is terminated at an early stage (Fig. 1c). Black regions (labeled as light blue circle in the inset of Fig. 1f) on $MoTe_2$ flakes were sometimes observed after the LV growth. Raman spectrum of the black region indicates that it is a mixture of elemental Te crystal and 2H $MoTe_2$, while other regions of the flake only show Raman features of 2H $MoTe_2$ (Fig. 1f). These black regions could be the residues of droplets. Furthermore, circular morphology of as-grown $MoTe_2$ as well as coffee rings suggest the presence of the original Te droplet and many $MoTe_2$ flakes forms from that (Fig. 1g and Supplementary Fig. 2). The $MoTe_2$ grown out of the liquid region indicates outward growth also exists, which could result from the reaction between in-situ vaporized Te from liquid reacts and Mo precursors (Fig. 1g, left panel). Moreover, we found that droplet sometimes crawls on the surface and $MoTe_2$ precipitates out, leaving a trace behind. The $MoTe_2$ shows the migration trace of the droplet, and the thicker region (whiter region) at the tip would be the location of the droplet residue (Supplementary Fig. 2). For other metal tellurides such as

GaTe system, flower-shaped GaTe was sometimes obtained with a droplet-like center and surrounding “petal” flakes (Fig. 1h). Some traces can be seen, which could be original Te droplet, now shrinking much in size (Fig. 1h). Raman spectra verify that the petals are the precipitated GaTe crystal (Supplementary Fig. 3). The GaTe flakes precipitate at the liquid-solid interface. The droplet does not completely deplete during the growth, then the liquid in the center condensed during the cooling process.

We start with $MoTe_2$ as an example to demonstrate the advantages of the LV method. Monolayer 2H $MoTe_2$ is a promising key material as the on-chip light source for next-generation silicon-based photo-electronics [14]. Moreover, monolayer 2H $MoTe_2$ provides a great platform for developing phase-change devices because of the reversible phase transition of monolayer 2H to 1T' $MoTe_2$ [12]. The 1T' $MoTe_2$ is the Weyl superconductor with an edge supercurrent [15], and monolayer 1T' is a quantum spin Hall insulator [16]. The synthesis of atomically thin $MoTe_2$ with controllable polymorphism is a huge challenge due to the fact that several crystal phases (2H [2,17], 1T' [15,16], 1T [18], T_d [19], *d*1T [20], and $2H_d$ [21]) with similar energies (energy difference between 2H and 1T' $MoTe_2$ <0.04 eV per unit formula) and tendency of decomposition during growth [2]. Since monolayer 1T' $MoTe_2$ is more stable than 2H $MoTe_2$ under Te deficiency [2], and Te vacancy is always generated during conventional growth [22], an efficient CVD method to synthesize monolayer 2H $MoTe_2$ is still lacking.

The synthesis of 2D $MoTe_2$ with specific phase can be realized *via* LV method by optimizing the thermodynamic and kinetic factors. Our phase-selective synthesis strategy is based on controlling Te and temperature which tunes the relative stability of the 2H and 1T' phases. Maintaining a Te enriched environment during growth to avoid Te deficiency should be a key point to obtain monolayer 2H $MoTe_2$. High-quality monolayer 2H $MoTe_2$ can be obtained using $MoCl_5$, H_2 and Te (details in Supplementary Information, Supplementary Figs. 4 to 8). To confine the as-grown $MoTe_2$ in monolayer form, the amounts of both Te and $MoCl_5$ were finely controlled. Low mass flux of $MoCl_5$ was realized by the ampoule tube design and the low amount of $MoCl_5$ precursor. The as-grown monolayer $MoTe_2$ flake shows hexagonal shape, a typical shape of 2H single crystals (with size ranging from a few to tens of micrometers, Fig. 2a). The step height of the flake is ~1 nm, consistent with the height of exfoliated monolayer 2H $MoTe_2$ (Fig. 2b).

Raman spectroscopy and polarized second-harmonic generation (SHG) spectroscopy were used to investigate the crystal phase, uniformity and optical anisotropy properties of the 2H $MoTe_2$ flake. Raman spectrum displays two peaks at 171 cm^{-1} (A_{1g} mode) and 236 cm^{-1} ($E_{2g}{}^1$mode) (Fig. 2c). The strong intensity of A_{1g} mode and absence of $B_{2g}{}^1$ mode (290 cm^{-1}) confirming the monolayer 2H nature of the flake [23]. The uniformly distributed color in both Raman intensity map of A_{1g} (Fig. 2d) and $E_{2g}{}^1$ (Supplementary Fig. 10) modes, together with no $B_{2g}{}^1$ signal over the whole flake region (Supplementary Fig. 10), suggest the uniformity of the monolayer flake. The SHG spectrum of the flake (Fig. 2e) displays a strong SHG signal and six-fold SHG pattern, consistent with the SHG feature of monolayer 2H $MoTe_2$.

Furthermore, the SHG mapping (Fig. 2e, inset) shows uniform intensity with hexagonal shape without boundary lines, indicating single crystal nature of the monolayer flake.

Monolayer 2H $MoTe_2$ film has also been successfully obtained *via* LV synthesis. The monolayer 2H film is uniform and continuous, with only the edge region of the sample showing discontinuity (Fig. 2f). Atomically resolved annular dark field scanning transmission electron microscopy (ADF-STEM) reveals the hexagonal atomic lattice of monolayer 2H $MoTe_2$ (Fig. 2g). X-ray photoelectron spectroscopy (XPS) measurement was conducted to examine the elemental composition, bonding types and phase purity of LV grown monolayer film. The high-resolution Mo 3d spectrum shows two prominent peaks at 228.3 eV ($3d_{5/2}$) and 231.5 eV ($3d_{5/2}$) which are attributed to the Mo-Te bonds (Fig. 2h). The two peaks at 573 eV and 583.4 eV in the Te 3d spectrum can also be assigned to the Mo-Te bonds (Fig. 2h). These features are consistent with that of bulk 2H $MoTe_2$ crystal and of CVD grown few-layer 2H $MoTe_2$ [17]. The XPS peaks for 1T' $MoTe_2$ were not detected in the sample, indicating that our CVD film is 2H $MoTe_2$ with high phase purity. Moreover, the atomic ratio between Mo to Te is ~1:2, suggesting the as-grown $MoTe_2$ is stoichiometric.

The LV grown monolayer 2H $MoTe_2$ exhibits excellent photoluminescence property. The photoluminescence (PL) spectrum of monolayer film shows a prominent PL peak centered at ~ 1135 nm (Fig. 2i), consistent with the direct band gap of monolayer 2H $MoTe_2$ at ~1.09 eV. Repeated measurements on various locations of the same film yield very similar position and intensity of the peak (Supplementary Fig. 11). The PL peak of the LV grown sample has a comparable intensity with the exfoliated monolayer sample, and different locations yield PL peaks with similar position and intensity, demonstrating high-quality and homogeneity for the LV grown monolayer 2H $MoTe_2$. Owing to the comparable direct bandgap with Si, superior optical property, as well as its 2D nature (without dangling bonds on the surface and can be easily integrate with Si), LV grown monolayer 2H $MoTe_2$ could be an excellent candidate for integration with Si photonics.

The LV technique can synthesize high-quality 2H $MoTe_2$ with controlled layer numbers via adjusting the amount of $MoCl_5$ precursor. The thickness of 2H $MoTe_2$ is found positively correlated with the amount of $MoCl_5$. Thus few-layer $MoTe_2$ is produced through increasing the amount of $MoCl_5$ in the ampoule. The step height of the hexagonal shaped flake is about ~2 nm, suggesting it is tri-layer $MoTe_2$ (Fig. 3a). Angle dependent polarized SHG displays six-folder pattern (Supplementary Fig. 12a), indicating the noncentrosymmetric nature of the flake. Given the flake is ~2 nm height, the flake should be tri-layer 2H $MoTe_2$. SHG mapping of the flake indicates there is no boundaries in the flake, suggesting the flake is single crystal $MoTe_2$ (Supplementary Fig. 12b). The Raman spectrum shows three peaks at ~171 cm^{-1} (A_{1g} mode), ~234 cm^{-1} ($E_{2g}{}^1$ mode), and ~290 cm^{-1} ($B_{2g}{}^1$ mode) (Fig. 3b). Since the out-of-plane $B_{2g}{}^1$ mode is Raman inactive for monolayer and bulk 2H $MoTe_2$, the flake should be few-layer 2H $MoTe_2$. The intensity maps of the A_{1g} peak and $E_{2g}{}^1$ peak display homogenous color over the flake region, suggesting high homogeneity of the few-layer 2H $MoTe_2$ flake (Supplementary Fig. S13). Since the ratio of $B_{2g}{}^1$/ $E_{2g}{}^1$

increases as the layer number of 2H $MoTe_2$ decreases, the uniformly distributed color over the flake in B_{2g}^1/ E_{2g}^1 map further indicates the flake has uniform thickness (Fig. 3c). High-resolution transmission electron microscopy (HRTEM) image shows a hexagonal atomic lattice without obvious defects. Moreover, selected-area electron diffraction (SAED) of the flake displays hexagonal symmetry pattern (Fig. 3d). These features are consistent with crystal structure of 2H $MoTe_2$, suggesting the high crystalline quality of LV-grown 2H $MoTe_2$. Transfer characteristics of a few-layer 2H $MoTe_2$ transistor displays ambipolar behavior with a current ON/OFF ratio of ~10^3 at room temperature (Supplementary Fig. 14). No obvious hysteresis is observed during the gate voltage scanning forward and backward. The near zero charge neutrality point indicates the as-grown $MoTe_2$ flake is intrinsic without obvious doping, in strong contrast with the heavy p-type doping 2H $MoTe_2$ grown by previous methods [13,17]. Therefore, LV grown $MoTe_2$ provides a good materials platform to investigate the intrinsic properties of 2H $MoTe_2$.

Phase-selective (2H or 1T') growth of $MoTe_2$ can be realized *via* LV method through tuning temperature or Te concentration. With less amount of Te pre-deposited on substrate and a lower growth temperature, high-quality 1T' $MoTe_2$ flakes will be obtained. Willow-leave like flakes were scattered on mica substrate with certain preferential directions (Fig. 3e). The elongated shape comes from the in-plane anisotropic feature of 1T' $MoTe_2$, with the long direction (preferential growth direction) along the zigzag Mo atomic chain. SAED from 1T' $MoTe_2$ shows rectangular pattern, consistent with the lattice structure of 1T' $MoTe_2$ (Supplementary Fig. 15). Raman spectrum of a flake displays several Raman peaks: A_g modes at 85 cm^{-1}, 115 cm^{-1}, 130 cm^{-1}, 164 cm^{-1}, 253 cm^{-1} and 272 cm^{-1}, as well as B_g modes at 93 cm^{-1} and 103 cm^{-1} (Fig. 3f). These features are consistent with the Raman spectrum of monolayer 1T' $MoTe_2$ [24]. Interestingly, the intensity of these modes is strongly dependent on the angle of the flake (Supplementary Fig. 16). Since Raman intensity is closely related to crystalline orientation because of the anisotropic nature of 1T' [25], the angle-dependent Raman intensity suggests that the flake is single crystal. The uniformly distributed color in the Raman intensity map of A_g mode at 164 cm^{-1} (Fig. 3g) further indicates the homogenous and single crystalline feature of the 1T' $MoTe_2$. In contrast, only sparse and small 1T' $MoTe_2$ flakes are obtained (Supplementary Fig. 17) *via* VSS growth.

XPS was utilized to characterize elemental composition and bonding types of the 1T' $MoTe_2$ sample. The Mo $3d_{5/2}$ peak at 228.1 eV and Mo $3d_{3/2}$ peak at 231.2 eV can be attributed to Mo-Te bonds. The strong Te $3d_{5/2}$ and Te $3d_{3/2}$ peaks at 572.7 eV and 583.1 eV are also assigned to Mo-Te bonds, consistent with bulk 1T' samples (Fig. 3h). There is no Mo oxide or Te oxide peaks in the high-resolution XPS spectra, indicating the CVD grown 1T' $MoTe_2$ is intrinsic without oxidation. The Te/Mo atomic ratio is estimated to be ~2.01, suggesting the CVD grown 1T' $MoTe_2$ is stoichiometric. The source-drain current versus voltage characteristic of the 1T' $MoTe_2$ grown from $MoCl_5$ (Fig. 3i) is linear and symmetric, with a sheet resistance of ~3200 Ω/sq, indicating the metallic nature of the flake.

The generality of the LV approach was demonstrated for the synthesis of diverse 2D metal tellurides, including transition metal ($MoTe_2$), IVA metal (SnTe) and IIIA metal tellurides (GaTe) with multiple crystalline phases (Fig. 4). β-SnTe is a topological crystalline insulator, and few-layer films show robust ferroelectricity at room temperature [26]. GaTe has extremely high photoresponsivity and good thermoelectric properties, which has promising applications in photonics and thermoelectric devices [27]. Liquid Te droplet works as a preferential reservoir for precursors from the gas phase, and subsequently as seed for the growth of 2D metal tellurides. We choose metal chloride instead of usual metal oxide to address the weak chemical reactivity of Te. The higher reactivity of chloride precursors leads to much faster reaction, synchronously avoid intermediate products and oxidation during growth. Moreover, the total oxygen-free growth condition can further ensure the high quality of as-grown metal telluride. For the synthesis of SnTe, we choose $SnCl_2$, H_2 and Te as precursors. After the LV growth, α-SnTe and β-SnTe were successfully obtained. The square shape of the flake (Fig. 4b) corresponds to the cubic crystal structure of β-SnTe. The Raman spectrum of the flake (Fig. 4c) shows two peaks at ~118 and ~139 cm^{-1}, consistent with the Raman features of nano-sized β-SnTe [28]. Interestingly, the low-temperature phase α-SnTe [29] is also stable at room temperature. The Raman peak at ~128 cm^{-1} (Fig. 4f) and EDS result (Supplementary Fig. 18) clearly prove that the trianglar flake is α-SnTe [29,30]. GaTe flakes are obtained from $GaCl_3$, Te and H_2. Four Raman peaks at ~ 125, 143, 160, 171 cm^{-1} (Fig. 4i) are the same as that of the GaTe flakes exfoliated from bulk crystal [27], indicating the as-obtained flakes are GaTe.

In conclusion, we have developed a universal LV method to synthesize 2D TMDs. The LV method provides an ideal way to continuously supply precursors, facilitates growth, suppresses decomposition, and enables growth of 2D materials/phase that are inaccessible through the conventional VSS growth. Moreover, LV-grown 2D materials show high quality due to minimum defects. The advantages of LV are demonstrated by synthesis of 2D metal tellurides with high quality, better controlled phase and stoichiometry, which were hard to synthesize previously due to low bonding energy, tendency for decomposition, and complex crystalline phases. In particular, monolayer 2H $MoTe_2$ film with superior properties was generated, thus enables diverse applications such as highly efficient near-infrared light-emitting diodes, near-infrared photodetectors, integration with silicon photonics, and phase-change devices. This method is of great significance for 2D metal tellurides with both fundamental and technological importance. We anticipate the LV strategy can be readily applied to synthesize many other high-quality quantum materials and heterostructures.

Methods

Synthesis of 2D metal tellurides

For the synthesis of $MoTe_2$, Te precursor (Sigma-Aldrich, 99.997%) was pre-deposited on substrates by spin-coating Te/chloroform solution (0.1 g Te/6 mL chloroform). The ampoule filled with $MoCl_5$ precursor (Sigma-Aldrich, 99.99%), substrates and Te powder were loaded into a tube furnace with a chamber of diameter 25 cm. The whole CVD system was purged with Ar and H_2 for 30 min before heating. Then, the

substrate and Te powder was heated to the growth temperature in 15 min under a gas flow (Ar 250 sccm, H_2 5 sccm). The ampoule was moved into the heating zone when reaching the growth temperature. The temperature of $MoCl_5$ during growth is ~200 ℃. After 10 min growth, the system was cooling down to room temperature by taking out the tube, and a mixture gas of Ar 300 sccm and 5 sccm is used to blow away reactants. For the synthesis of SnTe, $SnCl_2$ (Sigma-Aldrich, 99.99%) was filled in ampoule as the metal precursor. After purging the system with Ar and H_2 for 30 min, the substrate with pre-deposited Te and Te powder were heated to 650 ℃ in 15 min under a gas flow of Ar 100 sccm and H_2 100 sccm. Then $SnCl_2$ was pushed into furnace and kept at 650 ℃ for 20 min. The system was fast cooling down to room temperature after growth. GaTe was grown from $GaCl_3$ (Sigma-Aldrich, 99.99%), Te and H_2. The substrate and Te powder were first ramped up to 700 ℃ for 15 min (Ar 250 sccm, H_2 5 sccm), then ampoule filled with $GaCl_3$ was moved into the heating zone. The system was kept at 700 ℃ for 10 min growth under a mixture gas flow of Ar 100 sccm and H_2 100 sccm.

Characterization

Optical images were collected by optical microscopy (Axio Imager, Carl Zeiss). Raman characterization was performed with a Horiba Jobin Yvon HR800 system with a 633 nm excitation laser. The laser spot size was ~1 μm. AFM was conducted on Dimension 3100, Veeco Instruments Inc. in tapping mode. XPS was conducted on a PHI Versaprobe II XPS using Al Ka monochromated X-ray at low pressures of 1.3×10^{-8} Torr. XPS spectra were calibrated by shifting the highest peak in C 1s spectrum to 284.5 eV. PL spectra were collected using a home-built confocal microscope setup with a camera and an infrared spectrometer. SHG was collected by a photomultiplier tube using an 800 nm pulse laser excitation. SEM characterization was performed on Zeiss Merlin High-resolution SEM.

Declarations

Acknowledgments

We thank D. Feng and J. Zhang for insightful discussion, L. Ye and J. Checkelsky for providing facility to handle and store samples, G. S. Jung and T. Yang for theoretical analysis. X. Z. and L. Z. acknowledge the support from start-up funds of Shanghai Jiao Tong University. P.S. and J.K. acknowledge the funding from the Center for Energy Efficient Electronics Science (NSF Award No. 0939514), Q. J. and J. K. acknowledge the support from the STC Center for Integrated Quantum Materials, NSF grant no. DMR 1231319. Y. H. and N. Y. acknowledge the use of Princeton's Imaging and Analysis Center, which is partially supported by the Princeton Center for Complex Materials, a National Science Foundation (NSF)-MRSEC program (DMR-1420541).

Author contributions K. J. and L. Z. conceived the project. X. Z. and L. Z. conducted CVD growth, and carried out OM, AFM, Raman, XPS measurement. Y. H. performed TEM characterization. P. S., Y. L. and A. Z. fabricated devices and performed transport measurements. J. S. and Y. B. conducted optical

measurements. L. Z., X. Z. and J. K. analyzed the data and wrote the manuscript, with input from all authors.

Competing interests Authors declare no competing interests.

References

1 Desai, S. B. et al. MoS_2 transistors with 1-nanometer gate lengths. *Science* **354**, 99-102 (2016).

2 Cho, S. et al. Phase patterning for ohmic homojunction contact in $MoTe_2$. *Science* **349**, 625-628 (2015).

3 Radisavljevic, B., Radenovic, A., Brivio, J., Giacometti, V. & Kis, A. Single-layer MoS_2 transistors. *Nat. Nanotechnol.* **6**, 147-150 (2011).

4 M.-Y. Li, S.-K. Su, Wong, H.-S. P. & Li, L.-J. How 2D semiconductors could extend Moore's law. *Nature* **567**, 169-170 (2019).

5 Edelberg, D. et al. Approaching the intrinsic limit in transition metal diselenides via point defect control. *Nano Lett.* **19**, 4371-4379 (2019).

6 Dong, J., Zhang, L. & Ding, F. Kinetics of graphene and 2D materials growth. *Adv. Mater.* **31**, 1801583 (2019).

7 Li, H., Li, Y., Aljarb, A., Shi, Y. & Li, L.-J. Epitaxial growth of two-dimensional layered transition-metal dichalcogenides: growth mechanism, controllability, and scalability. *Chem. Rev.* **118**, 6134-6150 (2018).

8 Chiu, M.-H. et al. Metal-guided selective growth of 2D materials: demonstration of a bottom-up CMOS inverter. *Adv. Mater.* **31**, 1900861 (2019).

9 Fatemi, V. et al. Electrically tunable low-density superconductivity in a monolayer topological insulator. *Science* **362**, 926-929 (2018).

10 Wang, P. et al. Landau quantization and highly mobile fermions in an insulator. *Nature* **589**, 225-229 (2021).

11 Sajadi, E. et al. Gate-induced superconductivity in a monolayer topological insulator. *Science* **362**, 922-925 (2018).

12 Wang, Y. et al. Structural phase transition in monolayer $MoTe_2$ driven by electrostatic doping. *Nature* **550**, 487-491 (2017).

13 Zhang, Q. et al. Simultaneous synthesis and integration of two-dimensional electronic components. *Nat. Electron.* **2**, 164-170 (2019).

14 Bie, Y.-Q. et al. A $MoTe_2$-based light-emitting diode and photodetector for silicon photonic integrated circuits. *Nat. Nanotechnol.* **12**, 1124 (2017).

15 Wang, W. et al. Evidence for an edge supercurrent in the Weyl superconductor $MoTe_2$. *Science* **368**, 534-537 (2020).

16 Qian, X., Liu, J., Fu, L. & Li, J. Quantum spin Hall effect in two-dimensional transition metal dichalcogenides. *Science* **346**, 1344-1347 (2014).

17 Zhou, L. et al. Large-area synthesis of high-quality uniform few-layer $MoTe_2$. *J. Am. Chem. Soc.* **137**, 11892-11895 (2015).

18 Empante, T. A. et al. Chemical Vapor Deposition Growth of Few-Layer $MoTe_2$ in the 2H, 1T', and 1T Phases: Tunable Properties of $MoTe_2$ Films. *ACS Nano* **11**, 900-905 (2017).

19 Deng, K. et al. Experimental observation of topological Fermi arcs in type-II Weyl semimetal $MoTe_2$. *Nat. Phys.* **12**, 1105-1110 (2016).

20 Yuan, S. et al. Room-temperature ferroelectricity in $MoTe_2$ down to the atomic monolayer limit. *Nat. Commun.* **10**, 1775 (2019).

21 Zhang, F. et al. Electric-field induced structural transition in vertical $MoTe_2$- and $Mo_{1-x}W_xTe_2$-based resistive memories. *Nat. Mater.* **18**, 55-61 (2019).

22 Zhou, L. et al. Synthesis of high-quality large-area homogenous 1T' $MoTe_2$ from chemical vapor deposition. *Adv. Mater.* **28**, 9526-9531 (2016).

23 Yamamoto, M. et al. Strong enhancement of Raman scattering from a bulk-inactive vibrational mode in few-layer $MoTe_2$. *ACS Nano* **8**, 3895-3903 (2014).

24 Chen, S.-Y., Naylor, C. H., Goldstein, T., Johnson, A. T. C. & Yan, J. Intrinsic phonon bands in high-quality monolayer T' molybdenum ditelluride. *ACS Nano* **11**, 814-820 (2017).

25 Zhou, L. et al. Sensitive phonon-based probe for structure identification of 1T' $MoTe_2$. *J. Am. Chem. Soc.* **139**, 8396-8399 (2017).

26 Chang, K. et al. Discovery of robust in-plane ferroelectricity in atomic-thick SnTe. *Science* **353**, 274-278 (2016).

27 Huang, S. et al. In-Plane Optical Anisotropy of Layered Gallium Telluride. *ACS Nano* **10**, 8964-8972 (2016).

28 Salavati-Niasari, M., Bazarganipour, M., Davar, F. & Fazl, A. A. Simple routes to synthesis and characterization of nanosized tin telluride compounds. *Appl. Surf. Sci.* **257**, 781-785 (2010).

29 Brillson, L. J., Burstein, E. & Muldawer, L. Raman observation of the ferroelectric phase transition in SnTe. *Phy. Rev. B* **9**, 1547-1551 (1974).

30 Sugai, S., Murase, K. & Kawamura, H. Observation of soft TO-phonon in SnTe by Raman scattering. *Solid State Commun.* **23**, 127-129 (1977).

Figures

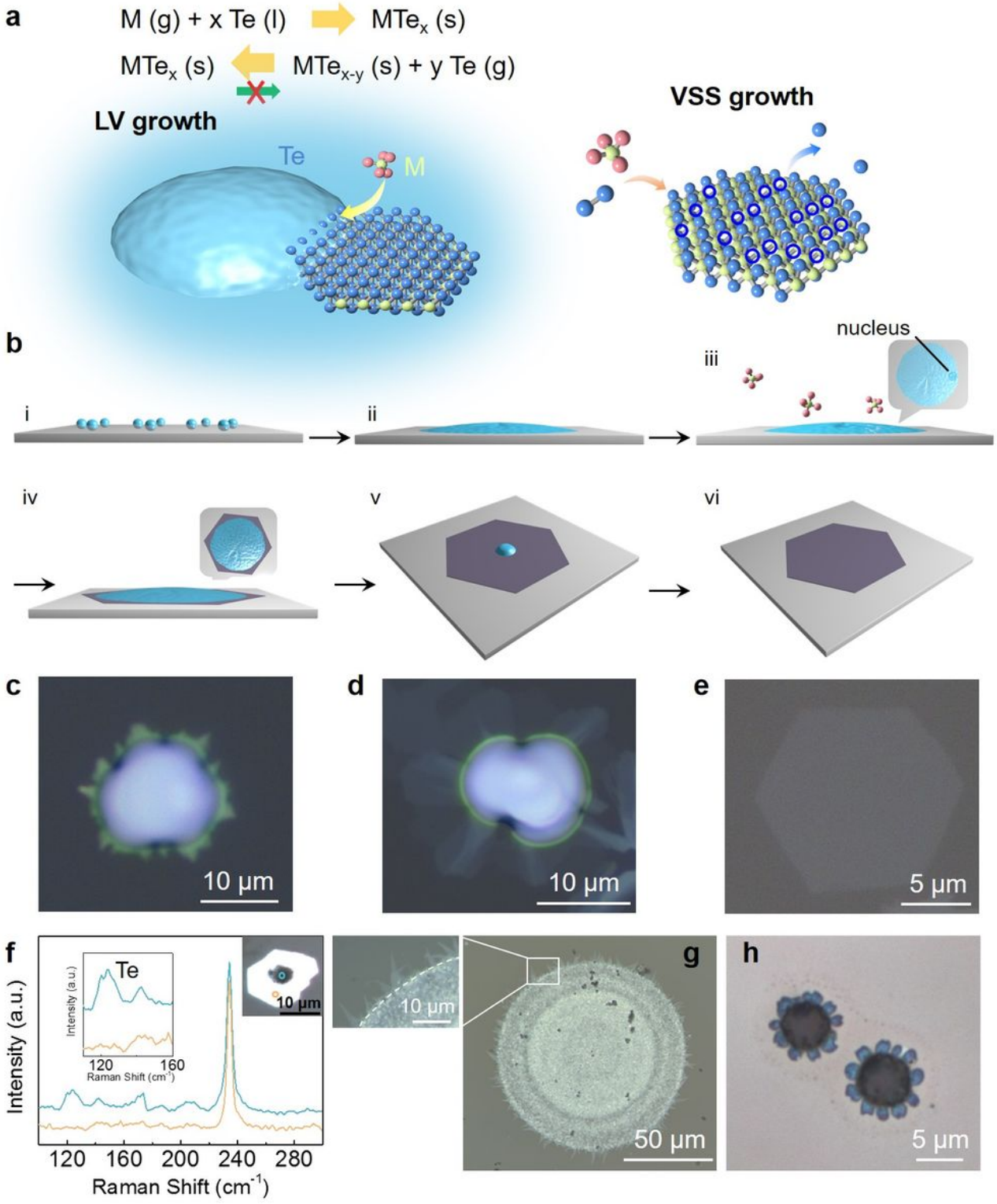

Figure 1

Schematic illustration and evidences of LV growth of 2D metal tellurides. (a) Left: Schematic of LV growth and involved reactions. Right: VSS growth of 2D crystal. The as-formed 2D crystal tends to decompose and forms vacancies (blue circles). (b) Depiction of LV growth process. (c to e) OM image of MoTe2 flakes with liquid at different growth stages (not the same flake). The (c) (d) (e) correspond to stages iv, v, and vi in (b), respectively. (f) Raman spectra of a 2H MoTe2 flake and the particle on top of it.

Inset: OM image of the corresponding 2H flake and the particle. (g) OM image of MoTe2 grown from liquid. The OM of edge region (left) shows that MoTe2 flakes can grow out from the liquid-solid boundary. Droplet edge is delineated by white line. (h) OM of LV grown flower-like GaTe. The black dots around GaTe should be the trace of the original liquid precursor.

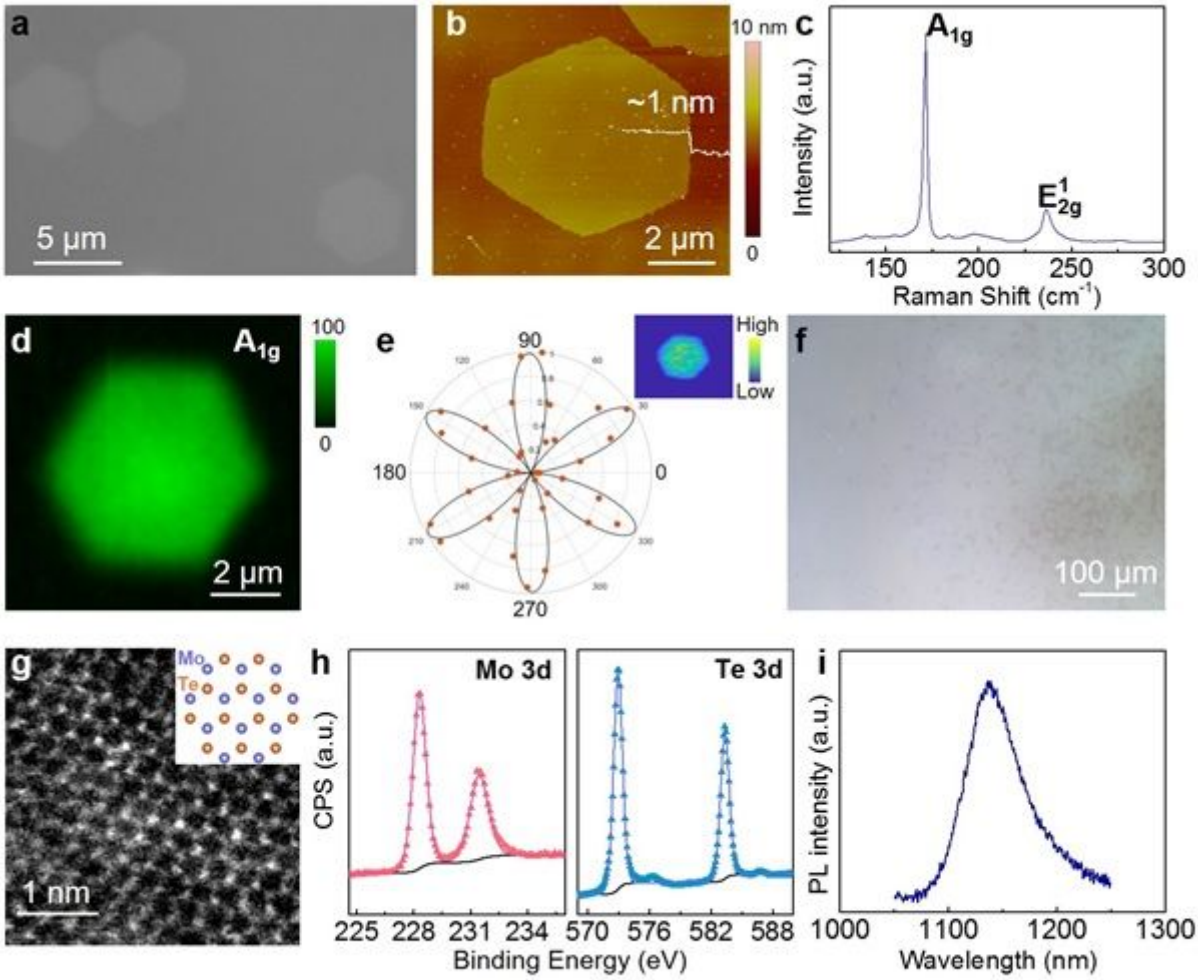

Figure 2

Characterizations of CVD-grown 2H monolayers MoTe2. (a) OM image of monolayer 2H MoTe2 flakes. (b) AFM image and height profile of a monolayer 2H MoTe2 flake. (c) Typical Raman spectrum of monolayer 2H MoTe2. (d) Raman mapping image for A1g peak of a monolayer 2H MoTe2 flake. (e) SHG intensity of monolayer 2H MoTe2 as a function of polarization angle. Inset: SHG mapping image of a monolayer 2H MoTe2 flake. (f) Optical image of the edge region of a monolayer 2H MoTe2 film. The white color denotes monolayer MoTe2 and the darker region is the bare mica substrate. (g) STEM image of monolayer 2H MoTe2. Inset: schematic atomic structure of monolayer 2H MoTe2. (h) XPS spectra of Mo 3d and Te 3d from a 2H monolayer MoTe2 film. (i) PL spectrum of monolayer 2H MoTe2.

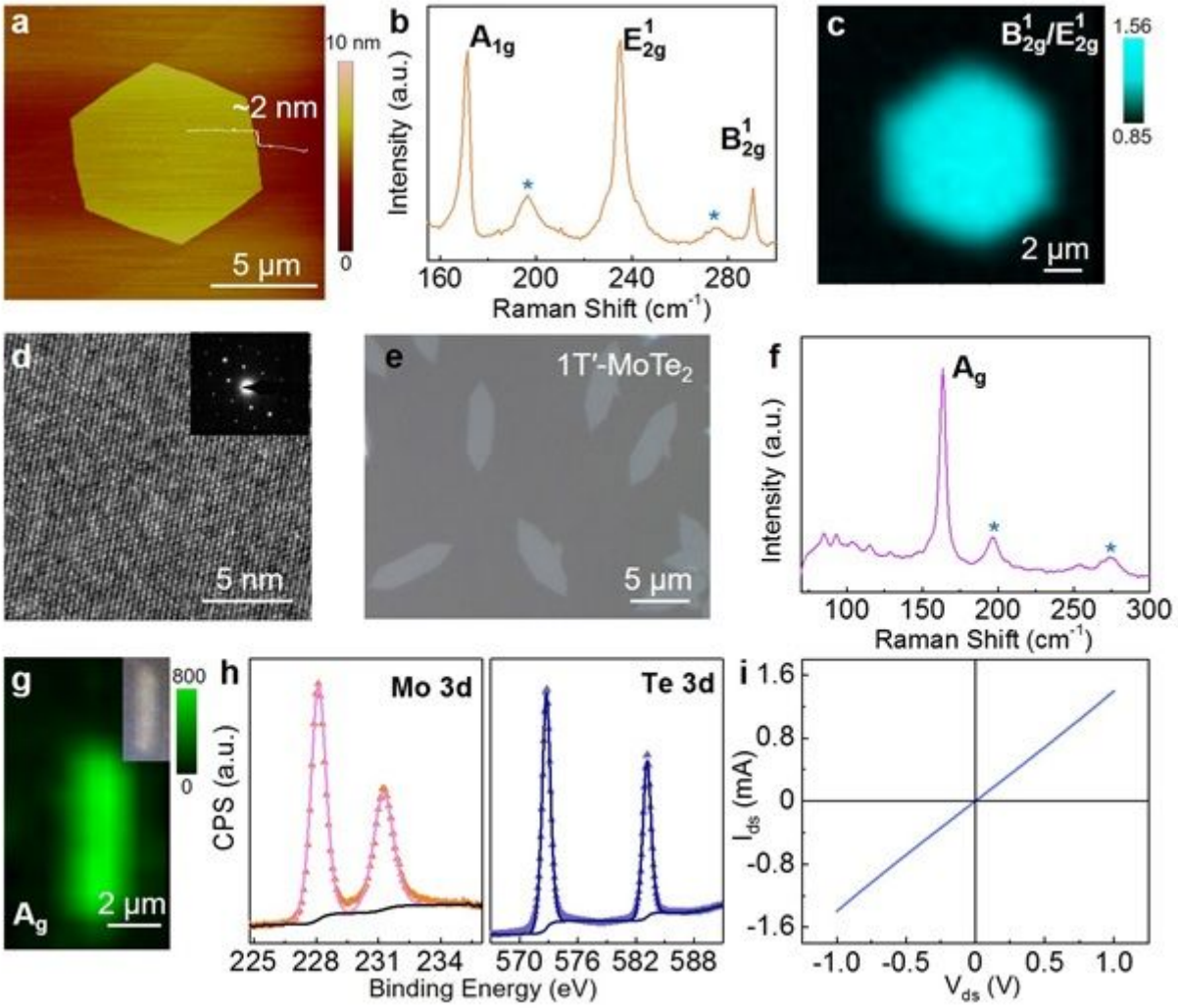

Figure 3

Characterizations of few-layer 2H and 1T' MoTe2. (a) Typical AFM image of few-layer 2H MoTe2. (b) Raman spectrum of few-layer 2H MoTe2. Peaks at 197 and 275 cm-1 come from mica substrate. (c) Raman mapping image (intensity ratio of B2g1 to E2g1) of an individual few-layer 2H MoTe2 flake. (d) High-resolution TEM and SAED pattern (inset) of few-layer 2H MoTe2. (e) OM of the CVD grown 1T' MoTe2 flakes. (f) Raman spectrum of a 1T' MoTe2 flake. The 197 and 275 cm-1 peaks attribute to mica substrate. (g) Raman mapping image of an individual 1T' MoTe2 flake. Inset: OM of the 1T' MoTe2 flake. (h) High-resolution XPS spectra of Mo 3d and Te 3d from a 1T' MoTe2 film. (i) Source–drain current (Ids) vs voltage (Vds) characteristics of a 1T' MoTe2 device.

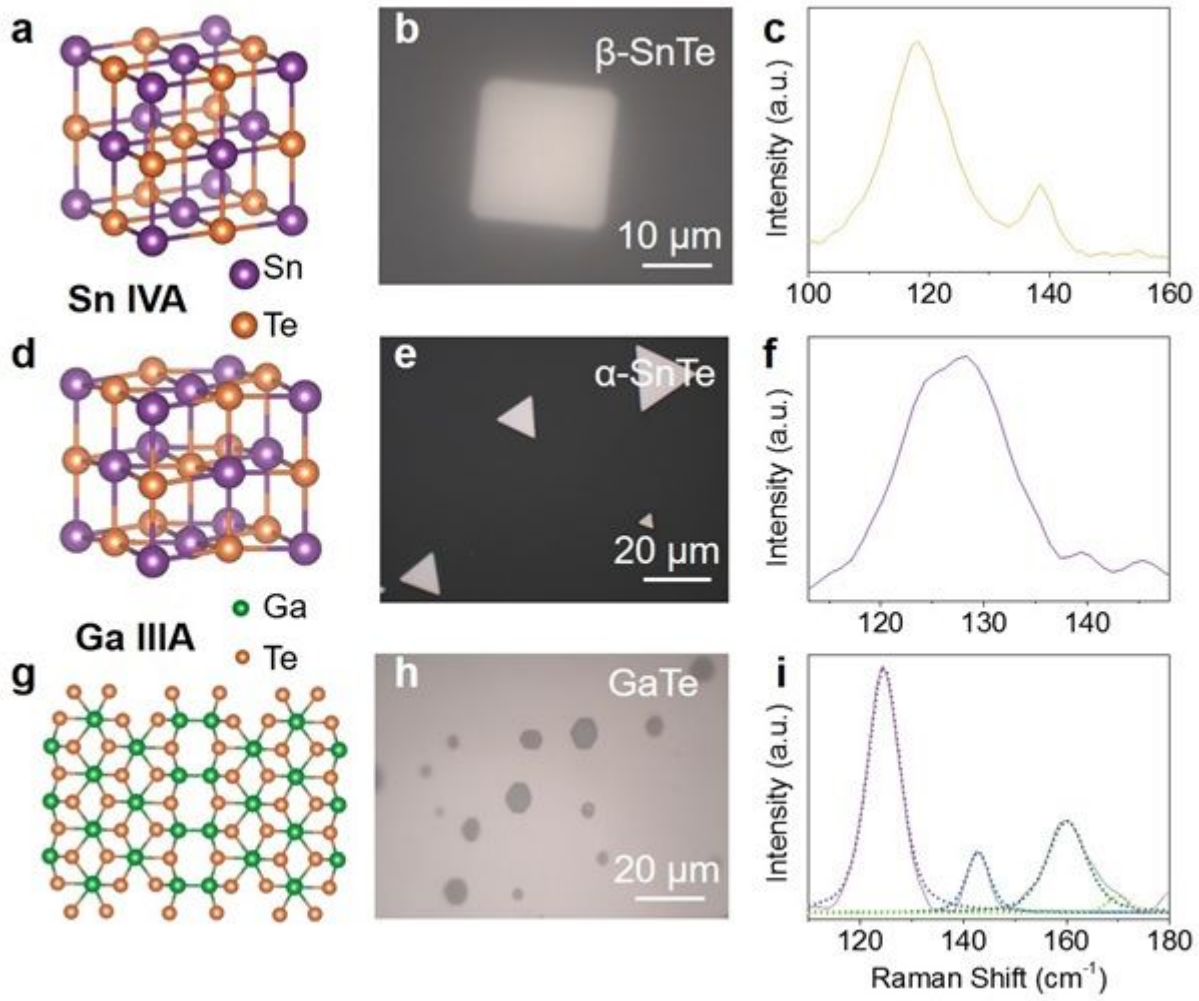

Figure 4

Generalization of the LV growth of 2D metal telluride. (a and d) Side views of the crystal structure of β- and α-SnTe. (b and e) Typical optical image of β- and α-SnTe flakes on mica substrates, respectively. (c and f) Raman spectra of β- and α-SnTe flakes. (g) Schematic of the GaTe crystal structure. (h) Optical image of the GaTe flake on mica. (i) Raman spectrum of the CVD-grown GaTe.

Supplementary Files

This is a list of supplementary files associated with this preprint. Click to download.

- Supplementaryinformation.docx